Geophys. J. Int. (2007) **169,** 216–232 doi: 10.1111/j.1365-246X.2006.03286.x

Combining InSAR and seismology to study the 2003 Siberian Altai earthquakes—dextral strike-slip and anticlockwise rotations in the northern India–Eurasia collision zone

Edwin Nissen,[1] Brian Emmerson,[2] Gareth J. Funning,[1]* Anatoly Mistrukov,[3] Barry Parsons,[1] David P. Robinson,[1] Eugene Rogozhin[4] and Tim J. Wright[1]†

[1]*COMET, Department of Earth Sciences, Parks Road, Oxford,* OX1 3PR, *UK. E-mail: ed.nissen@earth.ox.ac.uk*
[2]*Bullard Laboratories, Madingley Road, Cambridge* CB3 0EZ, *UK*
[3]*Trofimuk United Institute, Koptyug Pr.* 3, *Novosibirsk* 630090, *Russia*
[4]*Institute of Physics of the Earth, Russian Academy of Sciences,* 123810 *Moscow, B. Gruzinskaya* 10, *Russia*

Accepted 2006 November 4. Received 2006 October 23; in original form 2006 April 19

SUMMARY

The 2003 September 27 M_w 7.2 Siberian Altai earthquake was the largest to have struck the Altai mountains in more than seventy years, and was closely followed by two M_w 6.2 and 6.6 aftershocks. We use radar interferometry, seismic bodywaves and field investigations to examine the source processes of these earthquakes. The main shock of the initial earthquake ruptured a subvertical, ∼NW–SE striking dextral strike-slip fault. The fault was previously unrecognised; although it approximately follows the southwestern boundaries of two intermontane depressions within the interior northwestern Altai, it has very little topographic expression. A ∼NE-dipping $M_w \sim 6.7$ reverse subevent, possibly triggered by shear waves from the main shock, occurred ten seconds afterwards strike to the southeast. The later M_w 6.2 and 6.6 aftershocks were dextral strike-slip events which contributed further to deformation in the northwest part of the fault zone. However, interferometric and bodywave models disagree significantly on the source parameters of the earthquakes, in particular the total moment released and the dip of the fault planes. Trade-offs of fault dip with moment and centroid depth in the bodywave modelling can account for some, but not all, of these discrepancies. The interferometric data is unevenly distributed, containing many more data points on one side of the fault zone than the other; however, on the basis of calculations with synthetic data we rule this out as a reason for the discrepancies in fault parameters. The lower moment predicted by interferometry could be explained by the lack of coherent data close to the faulting, if slip was concentrated at very shallow depths. The dip yielded by the interferometric modelling might be influenced by lateral changes in elastic properties, although these would also affect the bodywave solutions. The earthquake sequence occurred close to recent palaeomagnetic measurements of late Cenozoic anticlockwise rotations. These suggest that the right-lateral strike-slip faulting that ruptured in the 2003 earthquakes accommodates regional ∼NNE–SSW shortening by rotating anticlockwise over time. The reverse subevent is a rare case of pure shortening perpendicular to the trend of the Altai range.

Key words: active tectonics, Altai, earthquake source parameters, faulting, InSAR, seismology.

1 INTRODUCTION

On 2003 September 27, a M_w 7.2 earthquake struck the northwestern Altai mountains in southern Siberia, close to the Russian borders with Mongolia, Kazakhstan and China (Fig. 1). Two large (M_w 6.2 and M_w 6.6) aftershocks occurred within 4 days of the main shock, and six smaller ($M_w \sim 5.0$) events in the following weeks. As well as the close temporal association, the earthquakes were clustered spatially, all within a ∼60 km long fault zone (Fig. 2).

Conventionally, such an earthquake sequence is studied using a combination of seismology and field observations. However, errors in hypocentral location can make it difficult to link individual seismic events with particular features of the surface deformation.

*Now at: Berkeley Seismological Laboratory, 377 McCone Hall, Berkeley, CA 94720-4760, USA.
†Now at: School of Earth and Environment, University of Leeds, Leeds LS2 9JT, UK.

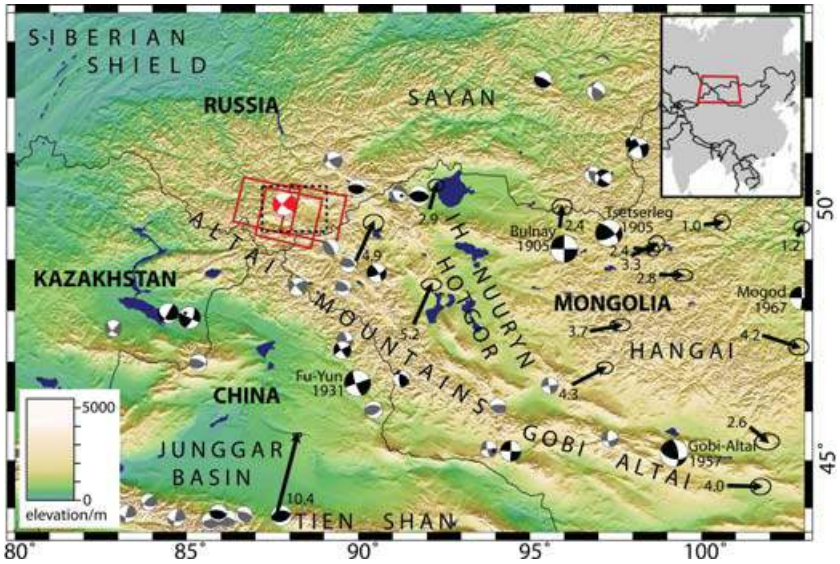

Figure 1. Shaded relief topography of the northern India–Eurasia collision zone, showing the position of the Altai mountains. The focal mechanisms of $M_w \geq 5$ earthquakes are shown, colour-coded, at the latitude and longitude given in the updated version of the Engdahl *et al.* (1998) catalogue. The red focal mechanism is our bodywave solution for the 2003 September 27 M_w 7.2 Siberian Altai main shock (for simplicity, none of the aftershocks are shown). Black mechanisms represent earthquakes studied using seismic waveforms or first motions (see Bayasgalan *et al.* 2005). Most of these occurred since the 1960s but four very large earthquakes from earlier in the 20th century are also included (the 1905 September 9 Tsetserleg, 1905 September 23 Bulnay, 1931 August 10 Fu-Yun, and 1957 December 4 Gobi-Altai earthquakes). Grey mechanisms are from the Harvard CMT catalogue (1977–2005). Arrows represent GPS velocities (mm yr^{-1}) relative to stable Eurasia with 95 per cent confidence ellipses (Calais *et al.* 2003). The red boxes indicate the frames of the three descending track interferograms used in this study, and the dashed black box shows the extents of Figs 2, 6, 8 and 14.

In recent years, Synthetic Aperture Radar Interferometry (InSAR) has provided a potential way around this problem. InSAR can provide a detailed map of surface deformation which, through modelling, can yield a set of earthquake source parameters. By comparing these source parameters with those determined using seismology, we can attempt to match detailed surface displacements to individual seismic events. However, just as seismology is limited by its poor spatial resolution, so interferometry lacks good temporal resolution. Because of the long intervals between consecutive passes used in interferometry, interferograms provide maps of total displacements over 35 days, or periods that are multiples of 35 days, for European Space Agency (ESA) satellites. When several earthquakes have occurred within this repeat interval, and are spatially close together, it can be difficult to distinguish individual coseismic ground movements. We investigate the 2003 Siberian Altai earthquakes to see if it is possible, by combining the spatial resolution of InSAR with the temporal resolution of seismology, to decipher the detailed history of a large, clustered earthquake sequence.

These particular earthquakes are interesting for another reason too. They occurred further northwest than any other large earthquakes in the Altai during the period of instrumental seismology, and the main shock was the largest to have hit the Altai since the M_w 7.9 Fu-Yun earthquake of 1931 (Fig. 1). The earthquakes thus provide important evidence for how shortening is accommodated in this area, the northernmost region of shortening in the India–Eurasia collision zone.

2 TECTONIC SETTING OF THE 2003 SIBERIAN ALTAI EARTHQUAKES

Lying around 2500 km north of the Himalaya, the Altai mountains comprise the most distal region of active continental shortening in the India–Eurasia collision zone (Fig. 1). GPS velocities show that at present, ∼7 mm yr^{-1} of SSW–NNE convergence is accommodated across the range (Calais *et al.* 2003). Shortening in the Altai thus makes a significant contribution toward the ∼35 mm yr^{-1} total India–Eurasia convergence, also constrained by GPS (Sella *et al.* 2002).

The Altai mountains trend northwest across the borders of Mongolia, China, Kazakhstan and Russia, and form a wedge shape narrowest in the southeast and widest in the northwest. Flat, low-lying and apparently undeforming areas border the Altai on three sides—the vast Siberian shield to the northwest, the Junggar basin to the south, and a collection of smaller basins known as Ih Nuuryn Hotgor (Depression of Great Lakes) to the east. Actively deforming mountainous regions lie northeast and southeast of the Altai. In the former case, the Sayan mountains see the transition between shortening in the Altai and extension in the Baikal region further east. In the latter, the Gobi Altai mountains accommodate NNE–SSW shortening across southern Mongolia. Though they join up with the Altai at their western end, the Gobi Altai are treated as tectonically distinct because earthquake focal mechanisms largely involve sinistral, not dextral, strike-slip.

The Altai mountains average ∼2500 m in elevation and reach a maximum height of 4506 m. They are not a typical intracontinental mountain belt, lacking frontal thrust faults and instead containing an anastomosing network of ∼NW striking dextral strike-slip faults (Cunningham 2005). These faults follow the structural grain of the range, inherited from the Palaeozoic accretion of continental fragments and arc terranes (Şengör *et al.* 1993). Many of the highest peaks are situated in the restraining bends of these faults, often around the edges of the range. Frequently, summits consist of distinctively flat-topped, uplifted peneplain surfaces. The onset of shortening in the Altai is estimated to be late Oligocene or early Miocene, based on a coarsening of continental sediments (Devyatkin 1974), and these peneplain surfaces suggest that there was

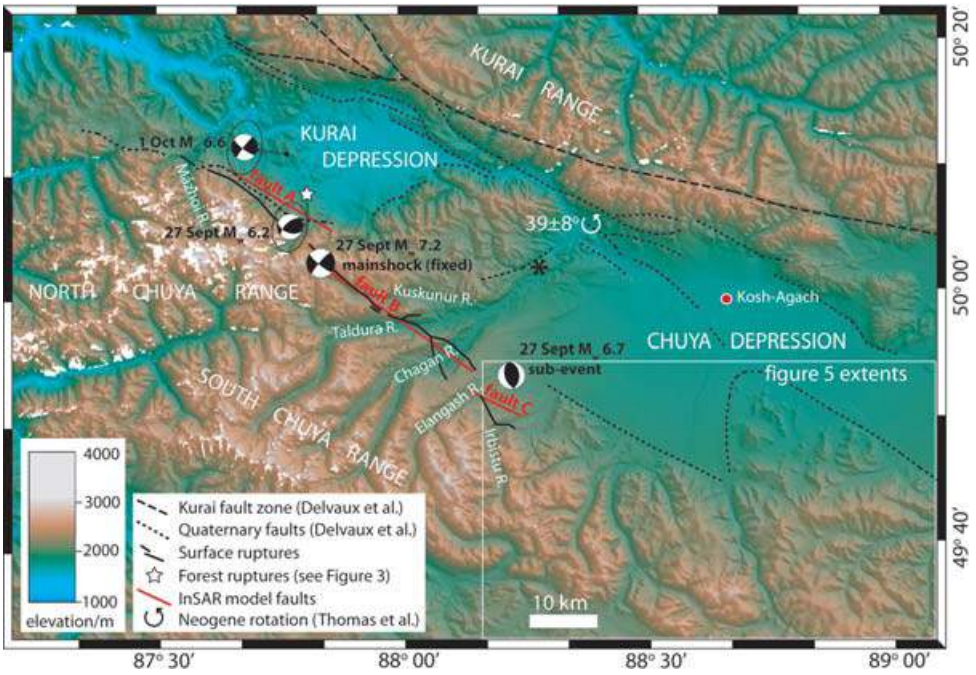

Figure 2. Shaded Shuttle Radar Topographic Mission (SRTM) digital topography of the epicentral region of the 2003 Siberian Altai earthquakes, in the local UTM zone (45) projection. The focal mechanisms are our bodywave solutions for the four M_w 6.2–7.2 events. The September 27 M_w 7.2 main shock is plotted in the position given in the updated version of the Engdahl *et al.* (1998) catalogue. Relative locations between this event and the September 27 M_w 6.2 and October 1 M_w 6.6 aftershocks were calculated using the Joint Hypocentral Determination (JHD) method (Dewey 1972). For the latter two events, arrows connect hypocentres from the updated version of the Engdahl *et al.* (1998) catalogue to 90 per cent confidence ellipses, relative to the fixed main shock, attained by the JHD method. Meanwhile the September 27 M_w 6.7 subevent is plotted in a fixed location, 32 km ESE of the main shock (see Section 4.3); its minimum-misfit location 32 km E of the main shock (marked with an asterisk) does not correspond with any significant interferometric deformation. Also shown are ruptures of the 2003 earthquakes mapped in the field, the surface traces of our InSAR model faults, and other Quaternary faults mapped in the area (Delvaux *et al.* 1995). The circular arrow shows the location of sediments yielding anticlockwise palaeomagnetic rotations from the study of Thomas *et al.* (2002); also marked is the Kurai fault zone, described by these authors as sinistral transpressional and to which they attribute the rotations (see Section 5).

little regional relief present beforehand (Cunningham *et al.* 2003).

In the 20th century, most large earthquakes in the Altai involved right-lateral strike-slip on ∼NW striking faults, the best known example being the 1931 Fu-Yun earthquake (M_w 7.9). Many other clearly active right-lateral faults have been mapped either in the field or using Landsat imagery (e.g. Devyatkin 1974; Tapponier & Molnar 1979). It has been suggested that these faults contribute to overall shortening by rotating anticlockwise over time (Baljinnyam *et al.* 1993; Bayasgalan *et al.* 1999, 2005). There have also been a few large thrust events, often involving ∼E–W striking faults towards either end of the Altai range. These earthquakes are thought to relate to the terminations of the NW striking, rotating strike-slip faults (Bayasgalan *et al.* 1999). Only one large earthquake in the 20th century (the M_w 5.2 event of 1998 November 21, at ∼49°N 89°E) involved pure shortening perpendicular to the trend of the Altai range.

The 2003 earthquake and its aftershocks struck the interior part of the northwestern Altai, just southwest of the Chuya and Kurai intermontane depressions (Fig. 2). The Chuya depression contains a good Cenozoic stratigraphic record, which has been used to infer its origins as an extensional basin in the Oligocene and Pliocene, and subsequent inversion along bounding thrusts starting in the late Pliocene (Delvaux *et al.* 1995). The clearest of these bounding faults, on Landsat images and in the topography, is the Kurai fault zone, which is described as undergoing sinistral transpressional deformation (Delvaux *et al.* 1995). Within the two depressions themselves several late Cenozoic faults have been mapped; palaeoseismological work has revealed that some of these faults ruptured in large earthquakes during the Holocene (Devyatkin 2000; Rogozhin *et al.* 1998a,b). Nevertheless, the faults on which the 2003 earthquakes occurred had not previously been recognized.

The Chuya depression was also the focus of a palaeomagnetic study in which 39° ± 8 anticlockwise rotations were measured in middle Miocene to early Pliocene sediments (Thomas *et al.* 2002). These measurements were taken just ∼30 km from the 2003 earthquakes, in the northwest part of the basin (Fig. 2). It has been proposed that ∼NW striking dextral strike-slip faults accommodate the NNE–SSW shortening across the Altai by rotating anticlockwise about vertical axes over time (Baljinnyam *et al.* 1993; Bayasgalan *et al.* 1999, 2005). So far, the Thomas *et al.* (2002) study is the only direct evidence that rotations do indeed occur in the Altai.

The first and largest of the 2003 earthquakes (M_w 7.2) happened on September 27 at 11:33 GMT, 17:33 local time. It was felt throughout southern Siberia and in much of Kazakhstan, as far away as Almaty, more than 1000 km to the southwest. Reports vary as to the extent of the resulting damage. It appears not to have directly led to a loss of life (unconfirmed reports claim three people died from heart attacks) or a great number of injuries, but according to some reports it left ∼1800 homeless in a number of villages in the Chuya and Kurai depressions. It also triggered landsliding in the mountains south of these basins, and flooding of the Chuya river. The first large aftershock (M_w 6.2) struck at 18:52 GMT on the same day, and a second major aftershock (M_w 6.6) followed on October 1

Figure 3. Field photos of earthquake ruptures in the southern Kurai depression, denoted by a star in Figs 2, 6 and 8. (a) 50° 08.273′N 87° 48.577′E, facing 030°. The fissure strikes 030° and is offset vertically by 40 cm, up to the SE. (b) 50° 08.342′N 87° 48.582′E, facing 180°. These fissures strike N–S along a small ridge. (c) Detail of a fissure on the same ridge as (b) with a pen for scale, pointing N (up). The fissure is 35 cm wide and offset vertically by 10 cm, up to the E. (d) Photo at 50° 08.532′N 87° 48.632′E, facing 005°, with notebook for scale. This fissure strikes ∼NW for 30 m along the western flank of another small ridge.

at 01:03 GMT. The M_w 6.6 event caused further damage to local villages and like the first earthquake was felt over a large part of southern Siberia. Several smaller events occurred in the following weeks, including six earthquakes of M_w 5.0–5.2. Hypocentres for all the $M_w > 5.0$ events are available in the updated version of the Engdahl *et al.* (1998) catalogue. The M_w 7.2 hypocentre is located in the mountains just south of the Kurai depression, with the two largest aftershocks ∼6 km (M_w 6.2) and ∼17 km (M_w 6.6) to the NNW (Fig. 2). Most of the $M_w \sim 5$ aftershocks are also placed in or close to the Kurai depression, with the exception of one event in the southern Chuya depression.

3 FIELDWORK AND LANDSAT IMAGERY

Field-based mapping of surface deformation was undertaken by three of the authors (ER, EN and AM), and revealed three principle sections of earthquake ruptures (Fig. 2). In the western part of the fault zone, EN and AM and (separately) ER mapped ruptures across the southern Kurai depression; it is likely that some of the deformation in this section was missed due to the dense forest vegetation in this area. In the central part, ER mapped deformation between the Kuskunur and Chagan valleys in the SW Chuya depression; this work was undertaken immediately after the earthquakes and is already published in Rogozhin *et al.* (2003). EN and AM later revisited this same section of surface faulting. Finally, further east in the SW Chuya depression, ER mapped ruptures between the Elangash and Irbistu rivers.

In the southern Kurai depression we used the InSAR measurements (Section 4.1) as a guide to search for earthquake ruptures. A heavily forested, ∼5 km wide incoherent area divides positive and negative line-of-sight displacements along the southern flank of the depression. When we traversed this region we found a number of en echelon, left-stepping extensional fissures (Fig. 3). Individual fissures trended ∼N–S and were up to ∼50 m long; they displayed vertical offsets of up to ∼50 cm and openings of up to ∼40 cm. The orientation of these fissures is consistent with right-lateral strike-slip on a ∼NW striking fault. Unfortunately, we could only follow them for ∼3 km along the overall strike of the fault zone before they were lost in the dense forest vegetation, and it is likely that more ruptures are present further NW and SE. The location of these ruptures is plotted as a star on Fig. 2 (and subsequent figures). Ruptures are also present further west, along the northern flank of the North Chuya range. These were mapped as far west as the Mazhoi valley, where

we measured a ∼20 cm dextral offset with uplift of the southwest side of the fault by ∼20 cm.

The most continuous section of ruptures (described already in Rogozhin *et al.* 2003) lies in the far southwest of the Chuya depression. These ruptures do not follow a topographic break of any sort, but cut obliquely across the Kuskunur, Taldura and Chagan valleys and the spurs between them. In the main part, they consist of spectacular ∼N–S striking extension fissures, up to 100 m long, 10 m wide and 3 m deep, and sometimes showing ∼0.5 m dextral offsets. Smaller ∼E–W striking push-up ridges, up to 50 m long and 2 m high, are also present. These extensional and compressional features are arranged en echelon in a zone striking ∼300° over a distance of ∼30 km, and again suggest an overall mechanism of right-lateral strike-slip on a ∼NW–SE striking fault.

In one place, on a high plateau between the Kuskunur and Taldura rivers, the ruptures can be followed more or less uninterrupted for ∼4 km. Here, we used the trace of the fault across the topography to estimate the dip of the fault (Fig. 4). We walked along the ruptures from a high saddle southeast of the plateau, down to and across the plateau itself, and up another saddle further northwest, measuring GPS positions and elevations of ruptures along the way. The plane defined by these *x*, *y*, *z* coordinates strikes 295° and dips 55–85° NE. Although there is a large uncertainty in absolute value of dip (due to the ruptures being distributed over a ∼100 m wide zone on the plateau), the field evidence does at least support a fault plane that dips to the northeast, rather than to the southwest. However, it should be noted that a curved fault plane that changes strike as it crosses the plateau could have produced the same pattern of ruptures, without requiring a dip to the northeast.

Finally, in the far eastern part of the fault zone we saw ruptures on the spur between the Elangash and Irbistu rivers. These display up to ∼1.2 m dextral offset and uplift of the northeast side by ∼0.65 m. In map view the trace of these ruptures is kinked, one segment striking ∼N–S and another striking ∼E–W.

We also studied Landsat images of the fault zone of the Siberian Altai earthquakes to look for geomorphic indicators of active faulting. There are no obvious features in the immediate vicinity of the ruptures mapped in the field. However, following their strike to the southeast, a distinct ∼50 km long lineation is visible, perhaps indicating the continuation of the active faulting which ruptured in the 2003 earthquakes (Fig. 5). In the northwest, it consists of a straight, north-facing scarp dividing hills to the southwest from a low, flat plain to the northeast (the southernmost part of the Chuya depression). Some streams appear to be incising southwest of the scarp, but stop doing so to the northeast, suggesting active uplift of the southwest side of the fault. If there is a reverse component to this part of the fault, this would indicate a fault dip to the southwest. Further southeast, the lineation enters hilly ground and is marked out by a series of very straight valleys.

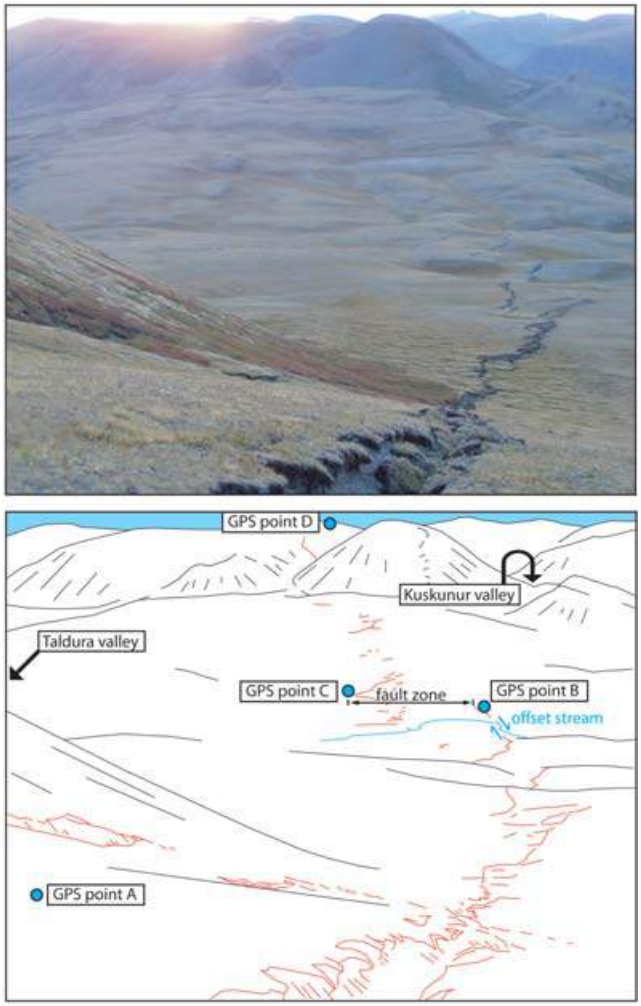

Figure 4. Field photo of earthquake ruptures on the plateau between the Kuskunur and Taldura rivers, taken from 49° 58.856′N 87° 59.223′E and facing 285°. Annotations are given on the sketch below the photo. The ruptures make a broad arc as they cross the plateau and rise to high saddles (at GPS points A and D) on either side. Such a pattern could be produced by a planar fault dipping to the right in the picture (to the NNE). On the plateau there is no single strand to the ruptures, which instead form en echelon fissures and push-ups over a ∼100 m wide zone between GPS points B and C. As a result we can calculate only a range of dip estimates, between 55° NNE (using the triangle ABD) and 85° NNE (triangle ACD).

4 EARTHQUAKE SOURCE PARAMETERS

In this section we investigate the source parameters of the 2003 September 27 earthquake and its two largest aftershocks using Synthetic Aperture Radar (SAR) interferometry and seismology. Three descending track interferograms provide us a map of cumulative line-of-sight displacements covering the earthquake sequence. We model these displacements using elastic dislocation theory and find that slip on three spatially separate fault segments can reproduce the data well. Using the same radar data we measure horizontal displacements (azimuth offsets), with which we compare our model derived from interferometry. We also study the sequence with seismology. We start by modelling the major seismic events using *P* and *SH* bodywaves, providing a second set of source parameters, independent of those attained through elastic dislocation modelling. We then determine the spatial pattern of the aftershock sequence using joint hypocentral determination (JHD). We find significant discrepancies between the InSAR and bodywave models.

4.1 SAR interferometry

SAR interferometry has proved an immensely powerful tool in studying earthquakes, enabling coseismic ground motions to be measured to subcentimetric precision and with unparalleled spatial

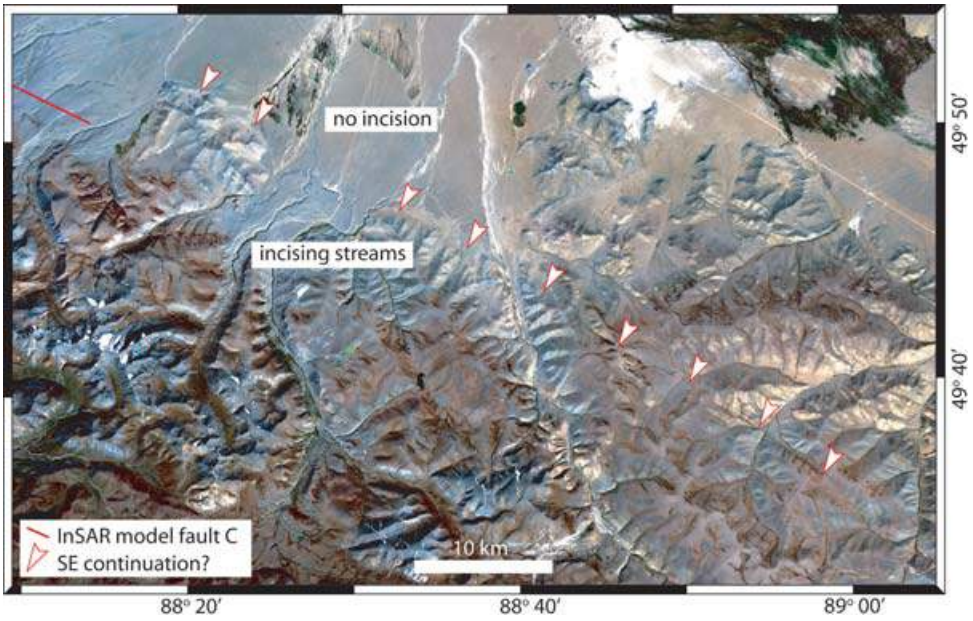

Figure 5. Landsat image (RGB 321) of the area southeast of the surface ruptures and InSAR model faults, showing a possible continuation to the active fault (picked out by arrows). In the northwest part of the map, the fault follows a N-facing scarp and streams only incise to the southwest. Further southeast, the fault follows a number of very straight valleys.

Table 1. Summary of Envisat data used to produce interferograms. The first image of each pair was acquired on Date 1, and the second on Date 2, separated by Δt days. The perpendicular baseline between the orbits in each pass is $B_\perp$ m., and the altitude of ambiguity H_a m.

	Pass	Track	Frame	Date 1	Orbit 1	Date 2	Orbit 2	Δt (d)	$B_\perp$ (m)	H_a (m)
Western	Desc.	434	2596	2003 September 11	08 003	2004 July 22	12 512	315	50	189
Central	Desc.	162	2601	2003 August 23	07 731	2003 December 06	09 234	105	166	57
Eastern	Desc.	391	2600	2003 September 08	07 960	2004 July 19	12 469	315	130	73

resolution. At present the principal satellite acquiring regular SAR measurements is the ESA Envisat platform, which was launched in 2002 but became fully operational only in 2003. The Siberian Altai earthquake was the first large continental earthquake for which prior Envisat Advanced Synthetic Aperture Radar (ASAR) data was available and interferometry possible.

We process the Envisat ASAR data (itemised in Table 1) using the JPL/Caltech ROI_PAC software (Rosen *et al.* 2004), to produce three adjacent, descending track interferograms, each with a centre-scene incidence angle of 23°. Precise orbits provided by ESA are used, but no further orbital adjustments are made. We remove the topographic phase contribution using the 3-arcsec (90 m) resolution Shuttle Radar Topographic Mission (SRTM) DEM (Farr & Kobrick 2000) and apply a power spectrum filter to smooth the interferograms (Goldstein & Werner 1998). The interferograms are shown in Fig. 6(a), overlaid on one other, and unwrapped and then rewrapped such that adjacent fringes differ by 10 cm in line-of-sight displacement. All three interferograms span the whole earthquake sequence and so cannot be used to distinguish between different aftershocks in time. Correlation is best in the low-lying, flat and sparsely vegetated Chuya depression, and in parts of the Kurai depression. However, the southern part of the Kurai depression is heavily forested and suffers from temporal decorrelation, while the mountains south of both depressions are very steep and display only patchy coherence. As a result, and with the added effects of steep deformation gradients, coseismic ground-shaking and land-sliding near the fault, the precise location of faulting within this area cannot be ascertained. Nevertheless, a ∼5 km wide, ∼60 km long strip of incoherence can be made out striking northwest across the southern margin of the Chuya and Kurai depressions; this strip separates line-of-sight displacements that are towards the satellite from those that are away from the satellite, and thus gives a rough indication of where the surface faulting must lie.

On the northeast side of this fault zone, line-of-sight displacements are towards the satellite and form a two-lobed pattern. The southeastern lobe, in the Chuya depression, contains the largest line-of-sight displacements, up to 1.9 m. In the northwestern lobe, in the Kurai depression, displacements reach 0.3 m, while the area between the two lobes contains displacements of up to 0.8 m. Southwest of the fault zone there is much less interferometric data, something we must bear in mind when modelling the earthquakes. Line-of-sight displacements in this part of the interferogram are away from the satellite and up to 0.3 m in magnitude. The overall pattern is consistent with dextral strike-slip, or uplift to the northeast and subsidence to the southwest, on a fault plane striking NW–SE. In addition, the greater number and closer spacing of fringes northeast of the faulting (a feature shown in more detail in Fig. 7) suggests that the fault plane dips to the northeast.

We reduce the number of data points from ∼2 million to ∼2000 for each interferogram using a quadtree decomposition algorithm (e.g. Jónsson *et al.* 2002). These data are then inverted using a downhill-simplex algorithm with multiple Monte Carlo restarts

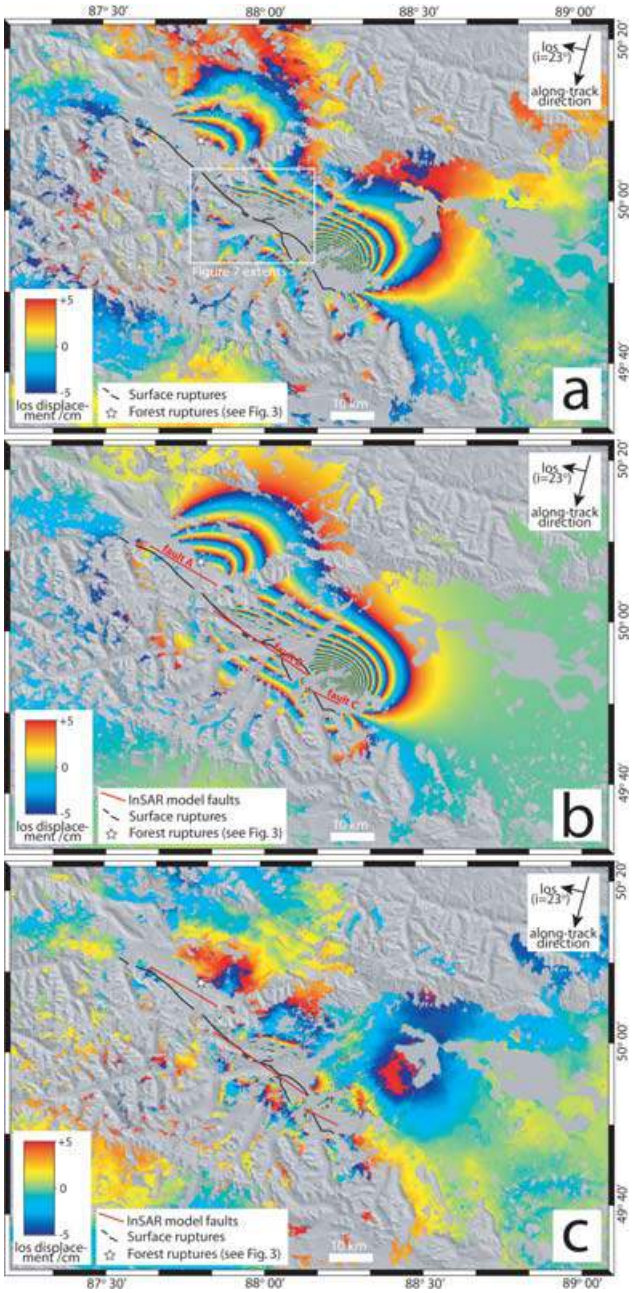

Figure 6. (a) Interferogram, unwrapped and then re-wrapped such that adjacent fringes differ by 10 cm in line-of-sight displacement. The figure actually contains three separate interferograms, each only covering part of the epicentral region, so we plot them together. They are overlaid on shaded SRTM topography. (b) Model and (c) residual interferograms, also shown wrapped such that adjacent fringes differ by 10 cm in line-of-sight displacement.

(Wright *et al.* 1999), to solve for uniform slip on a rectangular fault in an elastic half-space (Okada 1985); an elastic shear modulus of 3.23×10^{10} Pa and a Poisson ratio of 0.25 are used. The location, length, top and bottom depths, strike, dip, rake and amount of slip are all free to vary in the inversion. We find that a single fault plane cannot reproduce the interferometric data. This result is unsurprising for two reasons. First, it is impossible to draw a single straight line through the fault zone which can cleanly divide areas of positive displacements from areas of negative displacements. Secondly, uniform slip on a single plane cannot reproduce the distinctive double-lobed pattern of positive displacements northeast of the fault.

We experiment inverting the data using different numbers of faults, with all parameters free to vary. Our preferred model contains three faults; we find that this model is significantly better a two-fault model, but is not much further improved by the addition of a fourth fault. In this three-fault model, one segment accounts for the northwestern lobe of positive displacements, a second segment accounts for the central portion, and a third the southeastern lobe. The model parameters are given in Table 2, where (and from here on in) the northwestern model fault segment is called fault A, the central segment B and the southeastern segment C. Each fault segment has a moment of between ∼10 and ∼14 $\times$ 10^{18} N m, with the total moment (∼39 $\times$ 10^{18} N m) equivalent to a M_w 7.0 earthquake. The strikes (295–305°) and dips (57–70° NE) of the three faults are similar, and each involves oblique slip with right-lateral and reverse components. However, the reverse component on fault C is much higher than on the other two faults, lying closer to pure dip-slip than pure strike-slip. Because the model faults dip NE, the reverse components result in uplift to the northeast and subsidence to the southwest of the faults.

Standard deviations in the model parameters are also given in Table 2. These were estimated by inverting 100 data sets perturbed by realistic noise (with the same statistical properties as the atmospheric noise present in undeformed parts of the interferograms), one fault at a time (Parsons *et al.* 2006; Wright *et al.* 2003). Model source parameters for faults B and C are well constrained, partly because they are covered by two interferograms (tracks 162 and 391). In contrast, fault A is only covered by the western interferogram (track 434) and its 1σ errors are greater.

The model interferogram is shown in Fig. 6b and the residuals (a map of the difference between real and model interferograms) in Fig. 6c. Like the interferograms in Fig. 6a, they are shown wrapped such that adjacent fringes differ in line-of-sight displacement by 10 cm. There are few residual fringes, except for two areas; very close to the western end of fault C, and along the eastern half of fault B. In both cases, a fault whose slip could vary along strike, rather than ending abruptly as in the uniform slip model, might account for the residuals.

The surface traces of our model faults agree very well with the location of mapped ruptures (Fig. 6b). The best fit is between fault B and ruptures mapped in the far western Chuya depression. Fault A's location lies in between the two sets of surface ruptures mapped in the southern Kurai depression, around 2–3 km from either one, and the location of the mapped ruptures may reflect the splitting of this fault into parallel strands at shallow depths. Fault C's location lies very close to ruptures mapped SE of the Elangash river, although the kinked geometry of these ruptures is not required for our model to successfully reproduce the interferometric data.

4.2 Azimuth offsets

In addition to the ASAR phase measurements used in interferometry, the amplitudes of radar returns can also be used to study ground deformation (e.g. Michel *et al.* 1999). Horizontal displacements in the along-track direction are calculated by matching slave and master amplitude images to subpixel precision. These displacements, known as azimuth offsets, provide a further constraint on ground motion, independent of the line-of-sight phase changes measured by InSAR. We measure the azimuth offsets for the three Envisat ASAR scenes used in the InSAR. The displacements are shown in

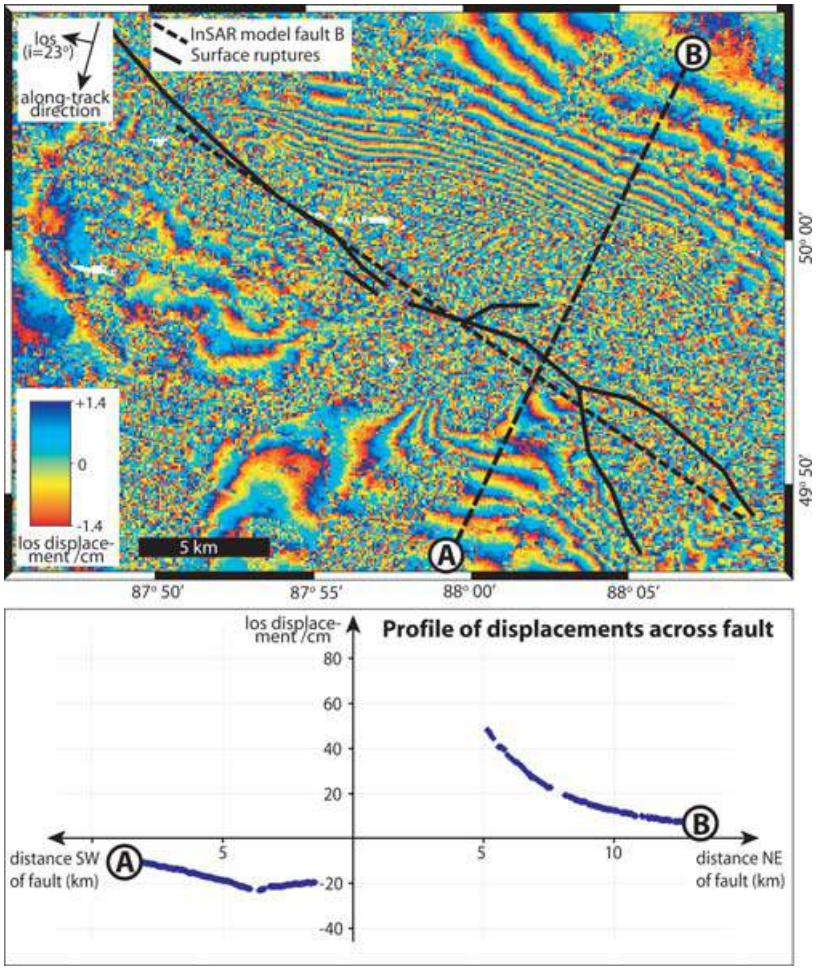

Figure 7. Detail of part of the western interferogram, before filtering and unwrapping (adjacent fringes differing by 2.8 cm in line-of-sight displacement). The amplitude of line-of-sight diplacements northeast of the faulting is much greater than that to the southwest; this is demonstrated on the profile below the interferogram, which shows unwrapped line-of-sight displacements along a transect from A to B. The asymmetry of this profile is consistent with a fault that dips to the northeast.

Table 2. Fault plane parameters from the inversion of interferometric data, shown with 1σ errors. Fault A is the northwestern segment, fault B the central segment and fault C the southeastern segment in the model. *Top* and *Bottom* refer to the top and bottom depths of the fault plane.

Fault	Strike	Dip	Rake	Slip (m)	Top (km)	Bottom (km)	Length (km)	Moment (N m)	M_w
A	$300.6^\circ \pm 2.2$	$59.5^\circ \pm 3.4$	$155.0^\circ \pm 6.5$	1.06 ± 0.14	0.7 ± 0.4	15.3 ± 1.1	17.6 ± 0.7	$10.2 \times 10^{18} \pm 0.7$	6.67
B	$304.7^\circ \pm 0.3$	$70.3^\circ \pm 0.5$	$140.1^\circ \pm 1.8$	1.54 ± 0.03	0.0 ± 0.0	10.4 ± 0.2	26.3 ± 0.3	$14.4 \times 10^{18} \pm 0.2$	6.77
C	$295.9^\circ \pm 0.3$	$56.6^\circ \pm 0.3$	$101.3^\circ \pm 1.3$	4.37 ± 0.04	1.3 ± 0.1	11.1 ± 0.1	8.5 ± 0.1	$14.0 \times 10^{18} \pm 0.2$	6.76

Fig. 8a, next to those predicted by our InSAR model (Fig. 8b). The data are noisy, due to false matches between slave and master pixels, and we cannot invert them as we did the interferograms. However, the azimuth offsets do not suffer from patchy coherence and the location of the faulting can be seen relatively precisely. We find that jumps in the values of azimuth offset agree with the location of faulting predicted by our InSAR model and mapped in the field.

4.3 Teleseismic bodywave modelling and earthquake relocations

The M_w 7.2 earthquake and the M_w 6.2 and M_w 6.6 aftershocks were widely recorded by stations of the Global Digital Seismic Network. We consider only those waveforms recorded teleseismically (in the distance range 30°–90°) in order to avoid complications from the Earth's crust and outer core. For each of the three events, we use the MT5 program (Zwick *et al.* 1994) to invert *P* and *SH* waveforms by a weighted least-squares method (McCaffrey & Abers 1988). Following the procedure of Molnar & Lyon-Caen (1989) we obtain the strike, dip, rake, centroid depth, seismic moment and source–time function of the best double-couple solutions. The focal mechanisms are shown in Figs 9, 11 and 12; the source parameters are given in Table 3 alongside those listed in the Harvard CMT catalogue, for comparison.

For the September 27 M_w 7.2 earthquake, the best fit to the data is achieved when we model it as a double event, the main shock being followed, 10 seconds later, by a smaller subevent. We allow the location of the subevent (the distance and azimuth between

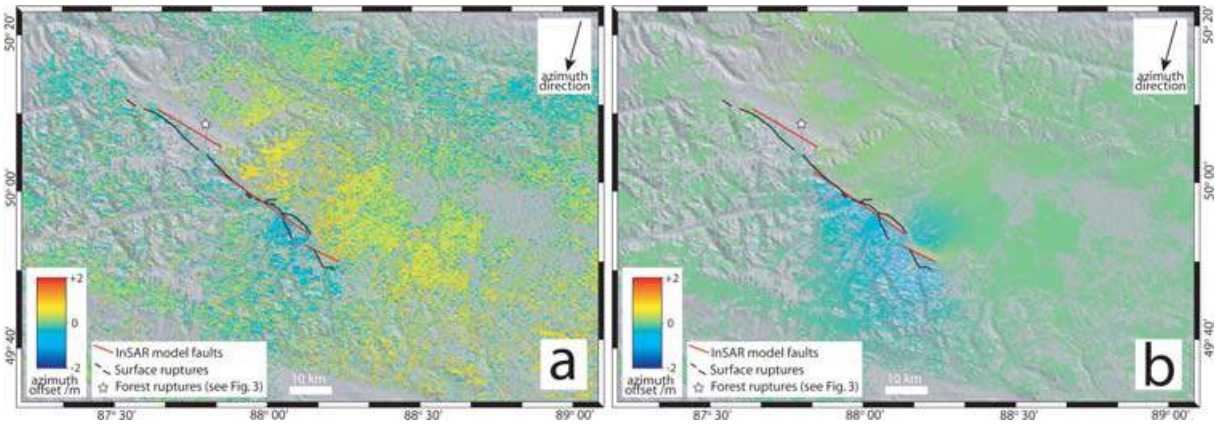

Figure 8. (a) Azimuth offsets, plotted over shaded SRTM topography. (b) Azimuth offsets predicted by our three fault InSAR model.

Table 3. Source parameters of the three largest events in the 2003 sequence determined through seismology; the depth listed is the centroid depth. Harvard CMT mechanisms are written in itallic (their centroid depths fixed), whilst those determined by inversion of *P* and *SH* bodywaves (Section 4.3) are in plain text. Origin times (GMT) are from an updated version of the Engdahl *et al.* (1998) catalogue, with the exception of the September 27 M_w 6.7 subevent. This was not listed separately in the catalogue and its timing was estimated along with its source parameters in the waveform inversion; its location was fixed relative to the M_w 7.2 main shock (see text).

Date	Time	Study	Strike1	Dip1	Rake1	Strike2	Dip2	Rake2	Depth	Moment (N m)	M_w
September 27	11:33:35	Harvard CMT	*131°*	*71°*	*158°*	*228°*	*70°*	*20°*	*15 km*	93.8×10^{18}	*7.2*
		This study	132°	82°	173°	223°	83°	7°	18 km	70.7×10^{18}	7.2
	+10 s	This study	163°	51°	82°	356°	40°	98°	6 km	16.2×10^{18}	6.7
September 27	18:52:47	Harvard CMT	*117°*	*67°*	*156°*	*217°*	*68°*	*25°*	*15 km*	4.5×10^{18}	*6.4*
		This study	111°	51°	143°	226°	62°	45°	12 km	2.5×10^{18}	6.2
October 01	01:03:25	Harvard CMT	*129°*	*85°*	*157°*	*221°*	*67°*	*5°*	*15 km*	11.3×10^{18}	*6.6*
		This study	127°	78°	176°	218°	86°	12°	7 km	8.5×10^{18}	6.6

subevent and main shock) to vary in the inversion. In the minimum misfit solution, the subevent lies ∼32 km from the main shock at a bearing of 089° (the asterisk on Fig. 2). This places it in an area lacking in significant interferometric deformation (comparing Fig. 2 with Fig. 6a), so the minimum misfit location is unlikely. By running several inversions for a variety of fixed offsets, we find that the subevent location is indeed poorly constrained; we see good matches between synthetic and real waveforms for offsets of 25–40 km, over which the azimuth changes from 120° to 088°.

We run another inversion with the subevent azimuth fixed to 120° and the distance fixed to 32 km; this places the subevent where we would expect it to plot, given the InSAR model and surface deformation. This model is shown in Fig. 9 and is our preferred solution. Waveforms for this model (plotted on the bottom line of Fig. 10) are not significantly degraded compared to the minimum misfit solution (middle line), but are significantly better than the best single event model (top line). This demonstrates the importance of including a subevent; although the subevent has a negligible effect on *SH* waveforms (YKW3 and UGM), it considerably improves the fit to the *P* waveforms (PET, UGM, FURI and DRLN), adding a second peak to the synthetic waveform which matches a peak present in the *P*-wave data.

The difference in the subevent mechanism between the minimum misfit solution and our preferred model reflects a broad minimum in the subevent misfit, with strong trade-offs in strike and depth (and to a lesser extent, rake) with distance and azimuth. A further point of note is that the distance/time between the main shock and subevent yields ∼3.2 km s^{-1}, a believable shear wave speed. The timing and position of the subevent are, therefore, consistent with rupture initiated by shear waves from the main shock.

From the fieldwork and InSAR, it is clear that faulting will correspond to nodal planes striking ∼NW–SE. The main shock thus involves mainly right-lateral strike-slip on a fault plane dipping very steeply to the southwest. The subevent involves mainly reverse motion, with only a small strike-slip component. Both nodal planes strike ∼NNW–SSE, with the ENE-dipping plane probably representing the fault (because all interferometric displacements towards the satellite lie northeast of the faulting).

The first large aftershock, also on September 27, is modelled as a single event (Fig. 11). In general there is a good fit between synthetic and observed waveforms, although for stations in the west the amplitudes of the two do not match well. The fault plane again strikes SE and dips to the SW, though less steeply than the largest event. The rake is intermediate between right-lateral strike-slip and reverse faulting.

The fit to the data for our model of the October 1 aftershock is worse than for the earlier earthquakes, especially for *P* waves in the west (Fig. 12). However, the solution cannot be significantly improved by adding a subevent of the same orientation and so we keep the single mechanism. Its minimum misfit solution is very similar to that of the largest event, but at a shallower depth. However, we find there to be a number of local minima close to this solution, within a few degrees of dip and rake and a few km of depth, and so the model is less well constrained than those of the earlier earthquakes.

Hypocentres for the 2003 earthquake sequence are available in the updated version of the Engdahl *et al.* (1998) catalogue. In this

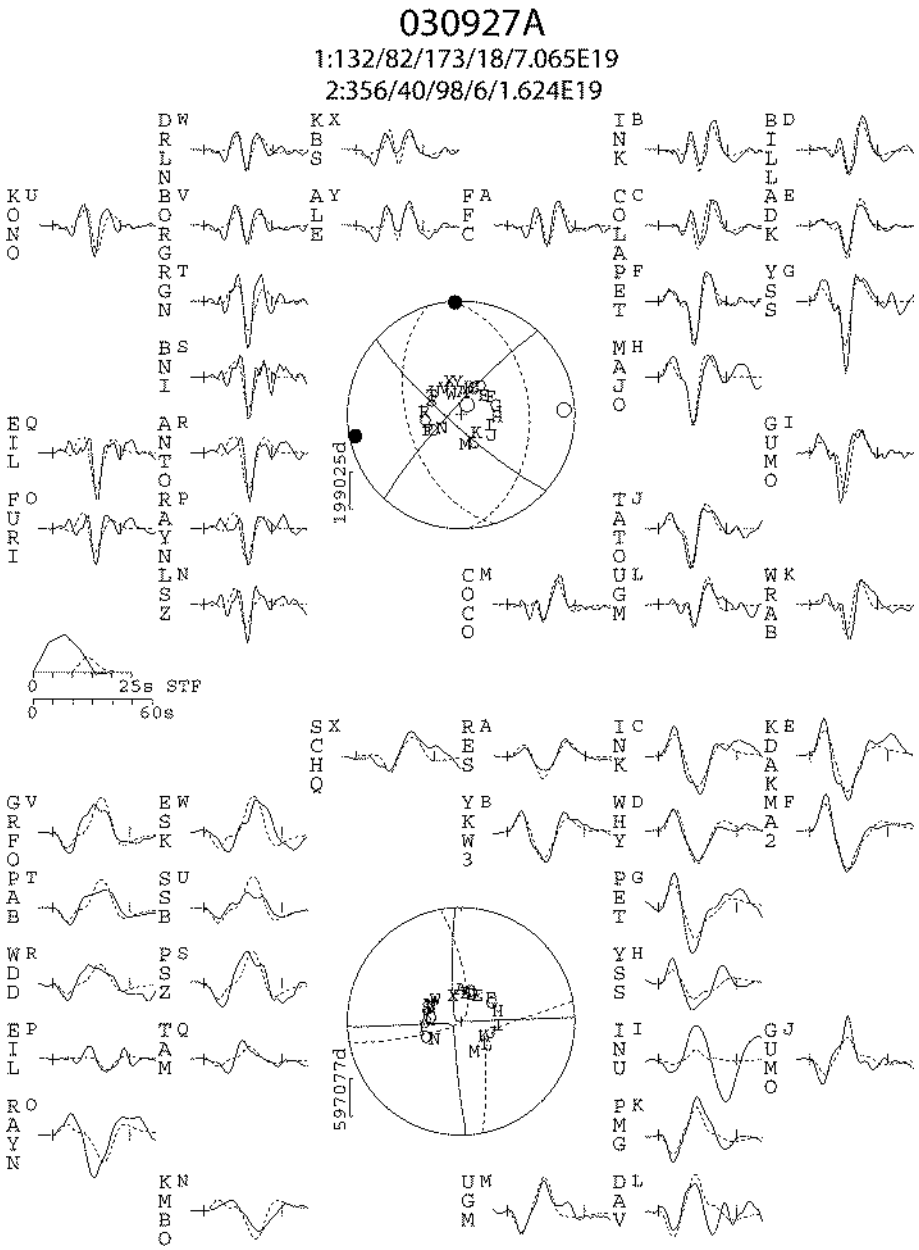

Figure 9. Our preferred model for the September 27 M_w 7.2 earthquake, calculated by inverting *P* and *SH* bodywaves for a point source in a half-space of $V_p = 5.9\ \mathrm{ms}^{-1}$ and $V_s = 3.4\ \mathrm{ms}^{-1}$. A subevent was included, fixed to a location 32 km from the main shock at an azimuth of 120° (see text). The focal spheres show *P* (top) and *SH* (bottom) nodal planes in lower hemisphere projections; solid nodal planes represent the main shock and dotted nodal planes represent the subevent, while the closed and open circles represent the *P*- and *T*-axes, respectively. Numbers beneath the header line are strike, dip, rake, centroid depth (km) and moment (N m) of the main shock (1) and subevent (2). Observed (solid) and synthetic (dashed) waveforms are plotted around the focal spheres; the inversion window is indicated by vertical ticks, station codes are written vertically and station positions denoted by capital letters. The STF is the source–time function, and the scalebar below it (in seconds) is that of the waveforms.

catalogue, the three largest earthquakes (modelled above) all lie in the northwestern part of the fault zone revealed by InSAR. However, these locations may be erroneous, perhaps through an inaccurate representation of the Siberian shield in the earth model used or some irregularity in local crustal structure. We use JHD (Dewey 1972) to calculate improved relative locations of the large earthquakes. These are shown, relative to the M_w 7.2 main shock and with 90 per cent confidence ellipses, in Fig. 2. Both M_w 6.2 and M_w 6.6 aftershocks lie northwest of the M_w 7.2 main shock, at distances of ∼7 and ∼20 km, respectively.

4.4 Comparing interferometric and seismic models of the earthquakes

We can now try to assign individual seismic events in the earthquake sequence to different parts of the fault zone. The M_w 7.2 main shock hypocentre lies ∼20 km SE of the M_w 6.6 aftershock and ∼32 km WNW of the M_w 6.7 subevent, so probably initiated in the central part of the fault zone. It most likely ruptured the entire length of the faulting (∼50 km, not unreasonable for a M_w 7.2 earthquake). The M_w 6.7 thrust subevent contributed further to deformation in the

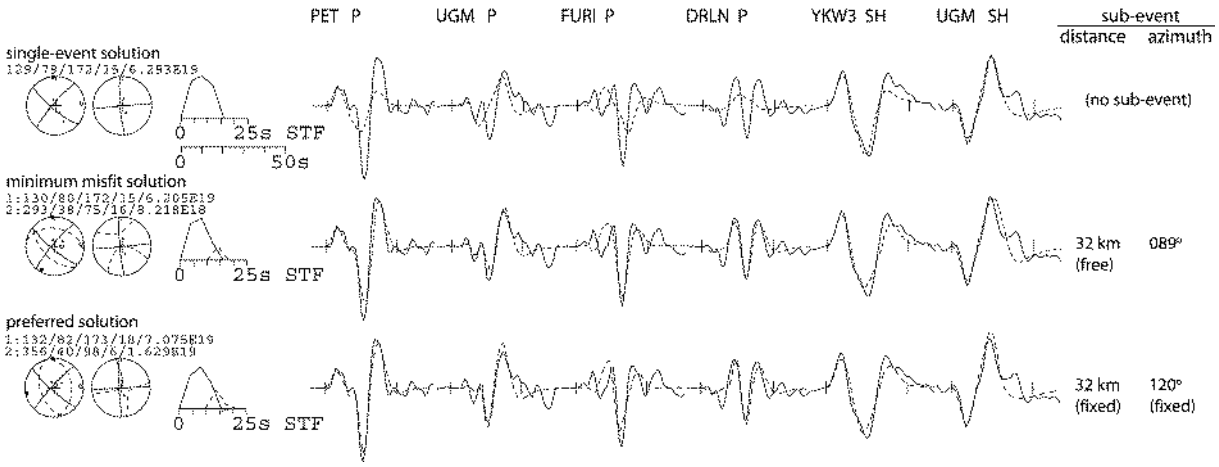

Figure 10. Bodywave models of the September 27 M_w 7.2 earthquake, showing the match between real (solid line) and synthetic (dashed line) waveforms for a selection of four *P* and two *SH* stations, indicated at the top of the figure. On the left-hand side, each model's *P* and *SH* nodal planes are plotted, in lower hemisphere projections and with solid and dashed lines again indicating the main shock and subevent, respectively. The model's strike, dip, rake, centroid depth (km) and moment (N m) are written above the focal spheres and the source–time function (STF) to the immediate right of them. The top line of waveforms shows the best-fitting solution for a single event, while the second line shows the minimum misfit solution, improved with the addition of a subevent. The bottom line shows our favoured model, in which the subevent location has been fixed to where we believe, from the InSAR and surface ruptures, it should lie.

southeast part of the fault zone, while the M_w 6.2 and 6.6 aftershocks added to deformation in the northwest. For this reason, and because the interferometry measures the cumulative deformation spanning the whole earthquake sequence, we are unable to isolate individual seismic events in the interferometric displacements. As a result we cannot directly compare the bodywave models of any individual event with the source parameters of any one InSAR model fault.

However, a more general comparison between the source parameters of the two models is still useful, and reveals some striking discrepancies. The combined moment of the three InSAR model faults (39×10^{18} N m) is less than half that of the four seismic bodywave models (98×10^{18} N m), despite the interferometric displacements including up to 9 months of post-seismic deformation (Table 1). In the central and northwestern parts of the fault zone, there are also striking discrepancies in fault dip and rake; the bodywave models of the M_w 7.2 main shock and M_w 6.6 and 6.2 aftershocks dip steeply southwest and two of these events are almost purely strike-slip, while InSAR model faults A and B dip steeply northeast and include a significant reverse component. Furthermore, the bodywave centroid depths (6–18 km) are generally deeper than the equivalent centroid depths of the InSAR model faults (5–8 km).

It is interesting and unusual to find such significant differences between interferometric and seismic models of the same earthquake sequence, and it is important to investigate the cause of these differences. We begin by investigating whether trade-offs between different source parameters (which affect both type of model) might account for the some of the differences in fault dip. We estimate the bounds of dip for each bodywave solution using the procedure of Molnar & Lyon-Caen (1989), inverting the data with fault dip fixed to a new value and seeing whether the fit between the synthetic and observed waveforms is noticeably degraded. When this is done for a series of fixed dip values, trade-offs with other source parameters will become apparent. Fig. 13 shows the dip test for the M_w 7.2 main shock as an example; from this we estimate a $\sim 10^\circ$ uncertainty in fault dip, with a dip of 90° (20° from that of InSAR fault B) within the bounds of error. This slightly reduces the discrepancy in fault dip between bodywave and InSAR models. Furthermore, we find that values of centroid depth and moment decrease significantly as the dip is forced towards the northeast. These trade-offs with fault dip could account for the discrepancy in centroid depth and some (but not all) of the discrepancy in moment. For the M_w 6.2 aftershock we estimate an upper bound of 61° SW for dip, which this time trade-offs positively with rake as well as with strike. For the M_w 6.6 aftershock, we estimate an upper bound of 90° in dip (the fit degrades as soon as the dip is forced towards the SW); trade-offs are difficult to ascertain because the differences in fit as a function of azimuth are so large (Fig. 12).

Trade-offs in InSAR model dip are also qualitatively assessed, by plotting the distribution of dips yielded by inverting 100 perturbed data sets against the distributions of other parameters. Only for fault A do we see clear trade-offs in dip; positively, with rake, slip, minimum depth and latitude, and negatively with length and longitude. However, these trade-offs are not large enough to explain the difference in fault dip.

The InSAR model faults are forced to dip towards to northeast because there are more fringes northeast of the faulting than to the southwest (Fig. 7). However, there is also much better coherence northeast of the faulting (in the Chuya and Kurai depressions) than to the southwest (in the steep Chuya ranges). As a result, more data points going into the inversion are from northeast of the faulting than from southwest of it. Such a bias in data coverage might influence the parameter values yielded by interferometric modelling, and we now investigate whether this could be so for the case of fault dip.

We start by inverting the interferometric data three more times, but with the dips of fault segments A and B fixed to values of 80° NE, 90° and 80° SW. All other parameters are free to vary in the inversions, including the dip of fault segment C. We also produce a fourth model, constraining the strike, dip and rake of faults A, B and C to lie very close to (within 5° for strike and dip, and 10° for rake) the values yielded by the bodywave inversions of the M_w 6.6 aftershock, the M_w 7.2 main shock and the M_w 6.7 subevent, respectively; other parameters are largely free to vary. The model parameters yielded by all four of these inversions are shown in Table 4.

Using the results of these fixed-dip inversions we produce model interferograms. These are shown in Fig. 14 alongside residuals, which increase progressively as the dip is forced further from the

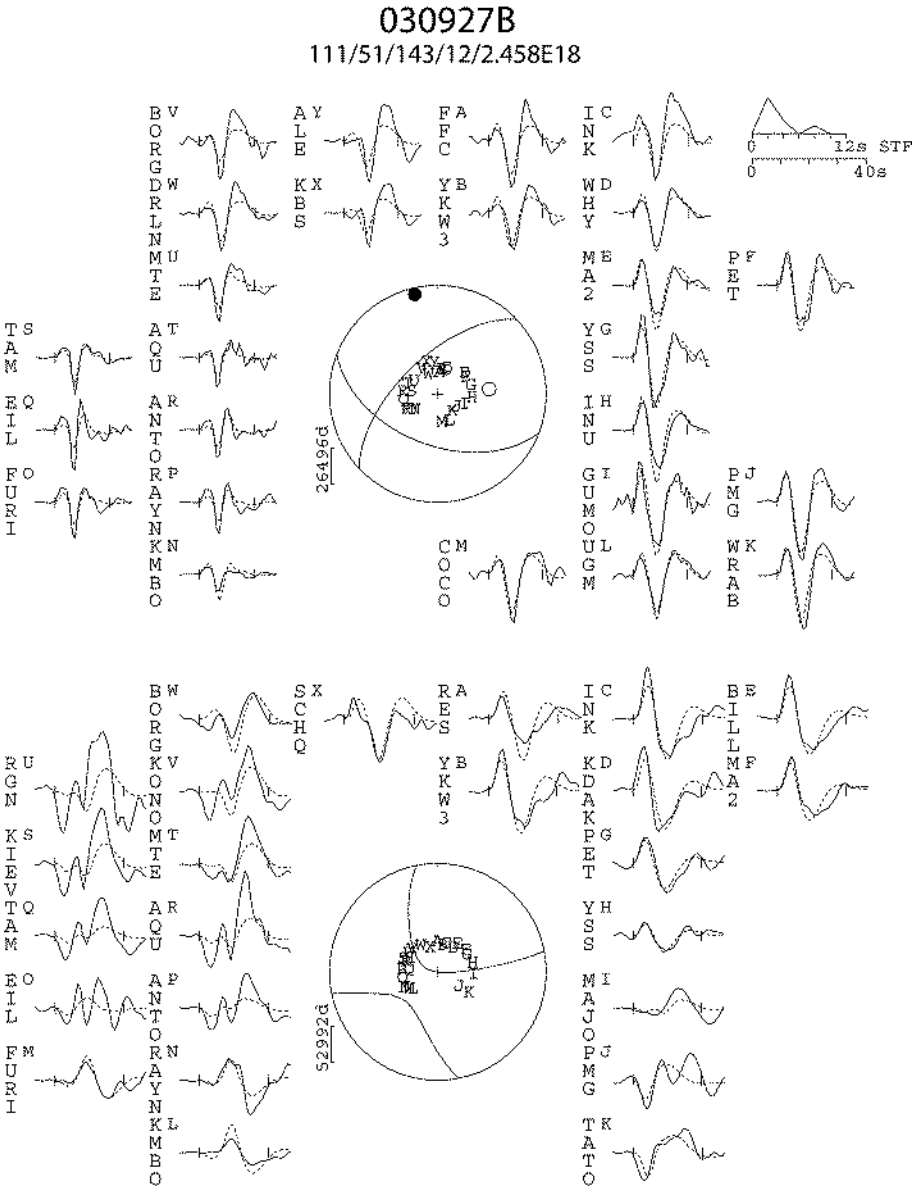

Figure 11. Minimum misfit solution for the September 27 M_w 6.2 earthquake. Layout is the same as in Fig. 9.

InSAR best-fitting solution and are especially large for model *iv*, where the strike, dip and rake are constrained to lie close to the bodywave solutions. We mask data corresponding to the incoherent parts of the real interferograms from these synthetic data sets, and add noise with the same statistical properties as the atmospheric noise present in the real interferograms. We then invert them in exactly the same fashion as is done in Section 4.1. In all four cases, the results of the inversions match the parameters (strike, dip, rake, slip, length, and top and bottom depths) used to make the synthetic data very closely. We are, therefore, confident that the bias in the data coverage does not affect the results of our interferometric modelling.

5 DISCUSSION

Although we have identified, for the first time, a large reverse slip event in the southeast of the fault zone, we have been unable to match individual seismic events with detailed interferometric displacements. Moreover, our seismic bodywave and interferometric models of the earthquakes disagree significantly on the earthquake source parameters, most strikingly in the values for moment (with the combined InSAR moment less than half that of the bodywave models) and dip (InSAR faults A and B dip steeply northeast, but minimum misfit bodywave solutions of the three strike-slip events dip steeply southwest). Trade-offs in the bodywave modelling can only partly account for these discrepancies, while the uneven interferometric data coverage cannot account for them at all. Instead, we should look at the assumptions made in the modelling.

In the interferometric modelling we have assumed uniform slip on each fault plane. One limitation of the interferometry is the ∼5 km wide strip of incoherence close to the surface faulting; if slip was not uniform but concentrated at very shallow depths (down to perhaps 2 km), then displacements within this incoherent area would be higher than expected. However, the greater moment resulting from these higher displacements would be missed by the InSAR

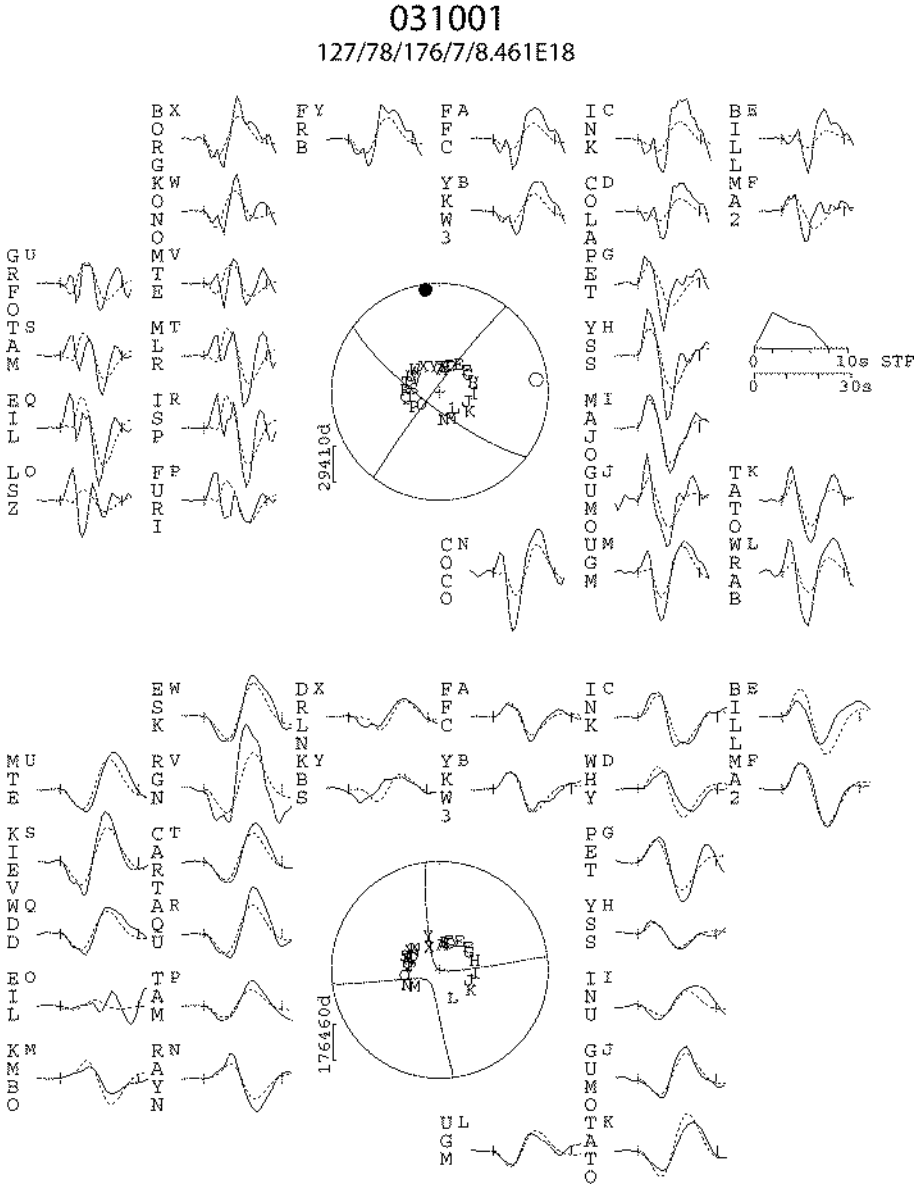

Figure 12. Minimum misfit solution for the October 1 M_w 6.6 earthquake. Layout is the same as in Fig. 9.

modelling. This is one obvious way to account for some of the discrepancy in moment. However, it does seem unlikely that enough slip could be concentrated at such shallow depths to account for all of the discrepancy in moment.

In the interferometric modelling we solve for slip in an elastic half-space; the elastic shear modulus is assumed to be a constant 3.23×10^{10} Pa. In reality, however, the elastic modulus is not uniform throughout the upper crust but will vary with lithology. There is a distinct change in lithology across the southern margins of the Chuya and Kurai depressions—to the south, the Chuya ranges are made of crystalline bedrock, while to the north, the Chuya and Kurai depressions contain ∼1200 and ∼500 m of Cenozoic sediments, respectively (Delvaux *et al.* 1995). The surface faulting approximately follows this change in lithology, so there is a higher elastic modulus south of the faulting than north of it, at least in the top ∼1 km of the crust. This might influence the number of fringes present either side of the faulting, with potentially more fringes than expected in the Chuya and Kurai depressions, where the elastic modulus is lower. If this was the case, the variation in elastic modulus could be forcing the apparent dip of the InSAR faults to the northeast, even if the real faulting was vertical or dipped steeply southwest.

A lateral variation in the elastic modulus of the upper crust would also influence take-off angles of seismic bodywaves, and so would affect the bodywave solutions too. Upper-mantle anisotropies are also known to exist beneath the Altai (Dricker *et al.* 2002) and these might also influence the seismology, although it is not clear exactly how.

Other observations of dip, from field measurements and the study of Landsat images (Section 3), are ambiguous. In different parts of the fault zone, there is evidence for both a dip to the northeast (between the Kuskunur and Taldura valleys, in Fig. 4) and a dip to the southwest (in the Mazhoi valley, and southeast of the surface ruptures, in Fig. 5). It is, therefore, possible that the strike-slip faulting changes dip along strike. A similar scenario has been envisaged for other large, continental strike-slip faults. Bodywave models of the

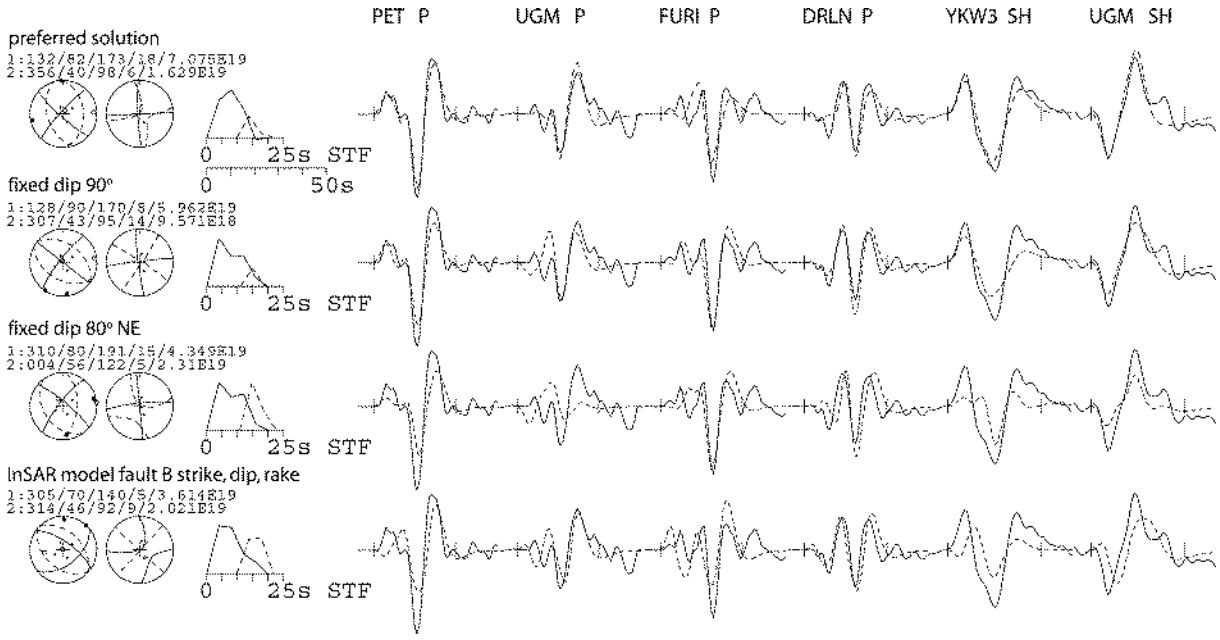

Figure 13. Dip test for the September 27 M_w 7.2 main shock, showing the match between real (solid line) and synthetic (dashed line) waveforms for a selection of four *P* and two *SH* stations. The top line shows our preferred solution (with subevent location fixed), in which the fault plane dips 80° SW. The second and third lines show solutions for fixed dips of 90° and 80° NE, respectively; in the third line (dip fixed to 80° NE) the depth was also fixed, to 5 km (the equivalent centroid of InSAR model fault B) because otherwise it was forced to zero. We estimate that the dip could lie as much as 10° from the minimum misfit solution—although the match for *P* waves at UGM is worse for a fixed dip of 90° than for the minimum misfit solution, the match at FURI is actually significantly better. The final line shows a model with strike, dip and rake fixed to the values of the InSAR solution for fault B; the fit between observed and synthetic waveforms is now significantly worse than in the first three lines.

Table 4. Fault plane parameters for four models of the 2003 Siberian Altai earthquakes, produced by inverting the interferometric data but with the dips of some faults fixed. Once again, fault A is the northwestern segment, fault B the central segment and fault C the southeastern segment in each model. In (i), the dip of faults A and B is fixed to 80° NE, in (ii), 90° and in (iii), 80° SW. In model (iv), the strike, dip and rake of all three fault segments were constrained to be close to the values of the corresponding bodywave models; strike and dip were allowed to vary by up to 5° and rake by 10° from the bodywave solutions. For (iii) and (iv), the length and bottom depth, respectively, had to be fixed at sensible values to ensure a realistic solution. The bottom three lines of the table show rms misfits for the Western, Central and Eastern interferograms. For comparison, the equivalent rms misfits for the best-fitting model (Fig. 6) are 2.77, 3.92 and 5.25 cm, respectively.

InSAR model		(i)			(ii)			(iii)			(iv)	
Fault	A	B	C	A	B	C	A	B	C	A	B	C
Strike (°)	322	305	295	327	305	294	151	125	293	129[a]	135[a]	351[a]
Dip (°)	80[b]	80[b]	57	90[b]	90[b]	58	80[b]	80[b]	61	79[a]	77[a]	45[a]
Rake (°)	145	146	96	161	152	94	185	186	90	172[a]	171[a]	88[a]
Slip (m)	1.27	1.61	4.63	2.10	1.79	4.81	2.22	3.43	5.06	4.90	3.08	5.43
Top depth (km)	1.8	0.0	1.4	2.6	0.0	1.5	0.7	0.0	1.7	0.0	0.0	3.1
Bottom depth (km)	25.9	9.7	11.4	15.3	8.9	11.5	15.3	6.1	11.9	13.7	15.0[b]	12.0
Length (km)	12.3	25.3	8.2	14.6	25.2	8.0	14.4	26.3[b]	8.1	18.3	29.8	7.7
Moment (N m $\times 10^{18}$)	12.3	12.9	14.4	12.7	12.9	14.7	15.4	18.0	15.4	40.3	46.0	17.1
M_w	6.66	6.68	6.71	6.67	6.68	6.72	6.73	6.77	6.73	7.01	7.04	6.76
rms misfit (W) (cm)		2.65			2.72			3.47			11.53	
rms misfit (C) (cm)		4.02			4.25			4.73			11.75	
rms misfit (E) (cm)		5.55			6.01			6.98			14.88	

[a]Parameters constrained during inversion to lie close to bodywave solution.
[b]Parameters fixed during inversion.

1997 May 10 Zirkuh, Iran earthquake (M_w 7.2) show four subevents varying in orientation along the strike of the fault (Berberian *et al.* 1999); this change in orientation is also seen at the surface, in observations of earthquake ruptures and geomorphology. Reversals in dip have also been identified along the Manyi fault in Tibet, in InSAR measurements of the 1997 November 8 Manyi earthquake (M_w 7.5) and in the geomorphology (Funning 2005). In both these cases the bodywave solution of the main shock alone says little about the orientation of the fault as a whole.

Irrespective of the dip, the faulting reactivated in the 2003 earthquakes lacks a clear topographic expression, explaining why it was previously unmapped. While the large strike-slip faults bounding the Altai range (e.g. the Ölgiy-Hovd, Har-Us-Nuur and Fu-Yun faults) are obvious in the topography, there may well be other active faults

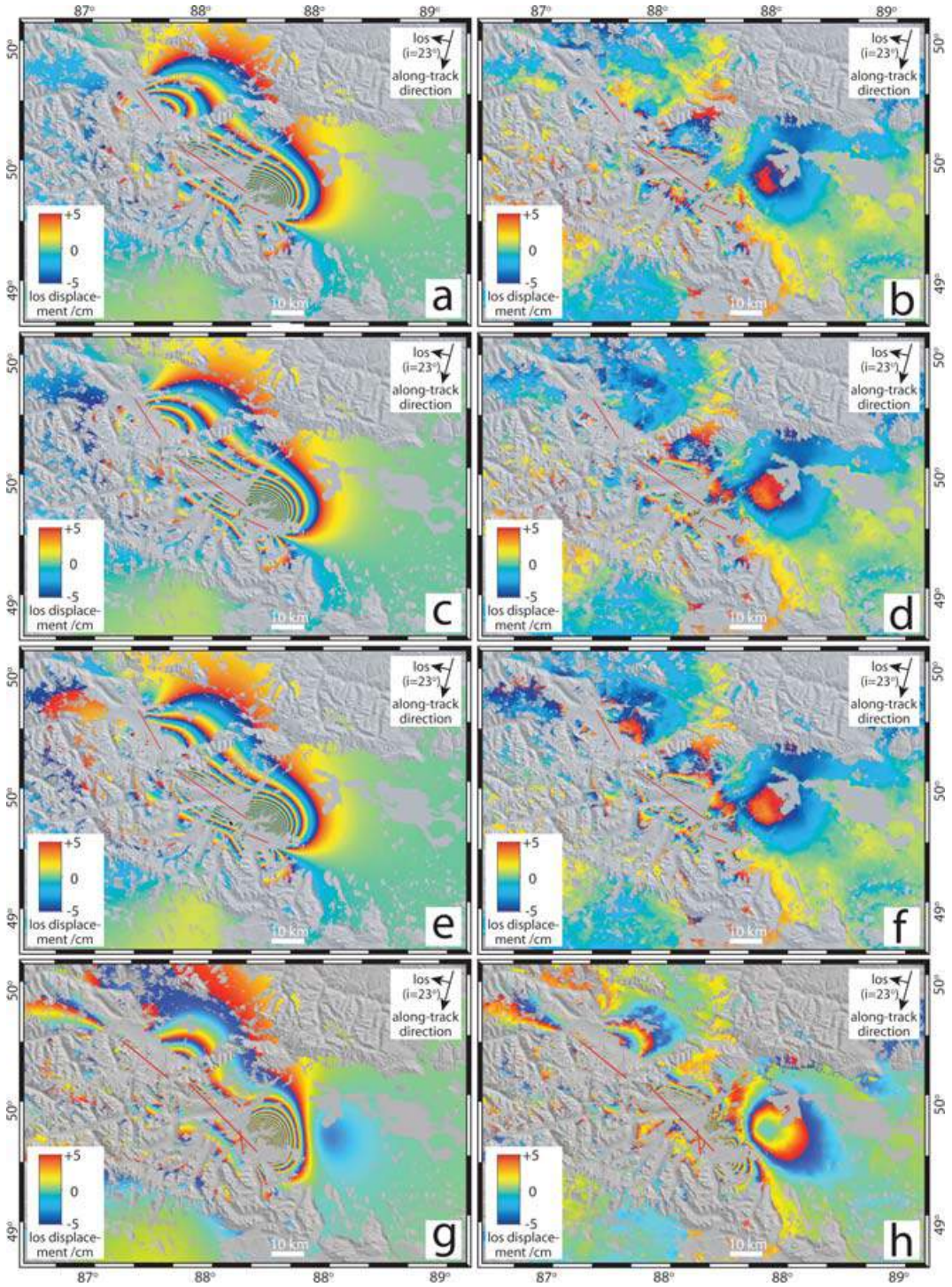

Figure 14. Model and residual interferograms produced by the inversion of interferometric data, and corresponding to the parameters given in Table 4. Faults A and B are constrained to dip 80° NE (a and b), 90° (c and d) and 80° SW (e and f). In g and h, faults A, B and C are constrained to have values of strike, dip and rake close to the corresponding bodywave solutions (see text).

in the interior of the Altai which have yet to have been mapped. The M_w 6.7 reverse subevent is also interesting because it acted as if to invert the Chuya depression; more normally, reverse-faulting in active continental mountain belts uplifts high ground relative to low ground.

Right-lateral strike-slip faults can accommodate shortening across the Altai if they and the slivers of crust between them rotate anticlockwise over time (Baljinnyam *et al.* 1993; Bayasgalan *et al.* 1999, 2005). The only study to have looked for palaeomagnetic rotations in the Altai mountains sampled upper Oligocene to Pleistocene clays and sandstones about 30 km northeast of the 2003 earthquake in the northwest Chuya depression (Thomas *et al.* 2002). Anticlockwise rotations of $39^\circ \pm 8$ were recorded in middle Miocene to early Pliocene sediments, though the authors suggest

that most of this occurred during the last 5 Myr. They attribute the anticlockwise rotations to the influence of the Kurai fault zone, which strikes E–W across the mountains north of the Chuya and Kurai depressions (Fig. 2). Although stream offsets across the Kurai fault in the northeast Chuya depression are consistent with dextral strike-slip, it is described in the literature as a sinistral transpressional fault (Delvaux *et al.* 1995); left-lateral motion on this fault zone is meant to have caused a domino-style rotation of the Chuya depression, giving rise to the palaeomagnetic rotations. However, the 2003 earthquakes strongly suggest that the rotations are instead associated with right-lateral shear along a fault zone striking ∼WNW–ESE across the southern margins of the Chuya and Kurai depressions. This style of deformation has been attributed to the Altai mountains further SE, in Mongolia and China, and should now be extended to the Siberian part of the range. There is one clear difference between the faults reactivated in the 2003 sequence and active faults further southeast, in the Mongolian and Chinese parts of the Altai; the former strike ∼300° whereas the latter strike ∼NNW. However, this probably reflects to the different orientation of structural grain in the Siberian part of the Altai (Dehandschutter 2001), rather than a change in the style of deformation.

6 CONCLUSIONS

The 2003 Siberian Altai earthquakes occurred on a segmented fault zone that had not previously been recognised. It is possible that there are other unmapped faults in the Altai capable of producing large earthquakes, particularly in the interior part of the range where their expression is not obvious in the topography. The 2003 sequence involved both right-lateral strike-slip and reverse movements, on fault segments striking ∼NW. The strike-slip segments rotate anticlockwise over time to accommodate the regional ∼NNE-directed shortening, while the reverse faulting represents a rare case of pure shortening perpendicular to the strike of the Altai range.

ACKNOWLEDGMENTS

Reviews by James Jackson and two others are gratefully acknowledged. We also thank Philip England, Richard Walker and Amgalan Bayasgalan for informative discussions, and to Alexandr Ovsyuchenko and Alexandr Marakhanov for help in mapping the surface ruptures. This work was supported by NERC funding of COMET (http://comet.nerc.ac.uk), a NERC studentship to EN and a Royal Society University Research Fellowship to TJW. Fieldwork was partly funded by a travel grant from University College, Oxford.

REFERENCES

Baljinnyam, I. *et al.*, 1993. Ruptures of major earthquakes and active deformation in Mongolia and its surroundings, *Geol. Soc. Am. Memoir.,* **181,** p. 62.

Bayasgalan, A., Jackson, J., Ritz, J.F. & Carretier, S., 1999. Field examples of strike-slip fault terminations in Mongolia, and their tectonic significance, *Tectonics*, **18,** 394–411.

Bayasgalan, A., Jackson, J. & McKenzie, D., 2005. Lithospheric rheology and active tectonics in Mongolia: relations between earthquake source parameters, gravity and GPS measurements, *Geophys. J. Int.,* **163,** 1151–1179.

Berberian, M., Jackson, J.A., Qorashi, M., Khatib, M.M., Priestley, K., Talebian, M. & Ghafuri-Ashtiani, M., 1999. The 1997 May 10 Zirkuh (Qa'enat) earthquake (M_w 7.2): faulting along the Sistan suture zone of eastern Iran, *Geophys. J. Int.,* **136,** 671–694.

Calais, E., Vergnolle, M., San'kov, V., Lukhnev, A., Miroshnitchenko, A., Amarjargal, Sh. & Déverchère, J., 2003. GPS measurements of crustal deformation in the Baikal-Mongolia area (1994–2002): Implications on current kinematics of Asia, *J. geophys. Res.,* **108**(B10), Art. No. 2501.

Cunningham, D., 2005. Active intracontinental transpressional mountains building in the Mongolian Altai: Defining a new class of orogen, *Earth planet. Sci. Lett.,* **240,** 436–444.

Cunningham, D., Dijkstra, A., Howard, J., Quarles, A. & Badarch, G., 2003. Active intraplate strike-slip faulting and transpressional uplift in the Mongolian Altai, in Intraplate Strike-Slip Deformation Belts, *Geol. Soc. Spec. Publ. London,* **210,** 65–87.

Dehandschutter, B., 2001. Study of the structural evolution of continental basins in Altai, Central Asia, *PhD thesis*, Vrije Universiteit Brussel, Belgium.

Delvaux, D., Theunissen, K., Van der Meer, R. & Berzin, N., 1995. Dynamics and paleostress of the Cenozoic Kurai-Chuya depression of Gorny-Altai (SouthSiberia): tectonic and climatic control, *Russ. Geol. Geophys.,* **35,** 31–51.

Devyatkin, E.V., 1974. Structures and formational complexes of the Cenozoic activated stage (in Russian), in Tectonics of the Mongolian People's Republic: Moscow, Nauka, 182–195.

Devyatkin, E.V., 2000. Inner Asia (in Russian), in Recent Tectonics, Geodynamics, and Seismicity of North Eurasia: Moscow, 92–100.

Dewey, J.W., 1972. Seismicity and tectonics of Western Venezuala, *Bull. seism. Soc. Am.,* **142,** 1711–1751.

Dricker, I.G., Roecker, S.W., Vinnik, L.P., Rogozhin, E.A. & Makayeva, L.I., 2002. Upper-mantle anisotropy beneath the Altai-Sayan region of central Asia, *Phys. Earth planet. Inter.,* **131**(3–4), 205–223.

Engdahl, E.R., van der Hilst, R. & Buland, R., 1998. Global teleseismic earthquake relocation with improved travel times and procedures for depth determination, *Bull. seism. Soc. Am.,* **3,** 722–743.

Farr, T. & Kobrick, M., 2000. Shuttle Radar Topographic Mission produces a wealth of data, *EOS, Trans. Am. geophys. Un.,* **81,** 583–585.

Funning, G.J., 2005. Source parameters of large shallow earthquakes in the Alpine-Himalayan belt from InSAR and waveform modelling, *PhD thesis*, University of Oxford, UK.

Goldstein, R.M. & Werner, C.L., 1998. Radar interferogram filtering for geophysical applications, *Geophys. Res. Lett.,* **25,** 4035–4038.

Jónsson, S., Zebker, H., Segall, P. & Amelung, F., 2002. Fault slip distribution of the M_w 7.2 Hector mine earthquake estimated from satellite radar and GPS measurements. *Bull. seism. Soc. Am.,* **92,** 1377–1389.

McCaffrey, R. & Abers, J., 1988. *SYN3: A program for inversion of teleseismic body wave form on microcomputers*, Air Force Geophysical Laboratory Technical Report, AFGL-TR-88-0099, Hanscomb Air Force Base, Massachusetts.

Michel, R., Avouac, J.-P. & Taboury, J., 1999. Measuring ground displacements from SAR amplitude images: application to the Landers earthquake, *Geophys. Res. Lett.,* **26**(7), 875–878.

Molnar, P. & Lyon-Caen, H., 1989. Fault plane solutions of earthquakes and active tectonics of the Tibetan Plateau and its margins, *Geophys. J. Int.,* **99,** 123–153.

Okada, Y., 1985. Surface deformation due to shear and tensile faults in a half-space, *Bull. seism. Soc. Am.,* **75,** 1135–1154.

Parsons, B. *et al*., 2006. The 1994 Sefidabeh (eastern Iran) earthquakes revisited: new evidence from satellite radar interferometry and carbonate dating about the growth of an active fold above a blind thrust fault, *Geophys. J. Int.,* **164,** 202–217.

Rogozhin, E.A., Bogachkin, B.M., Nechaev, Yu.V. Platonova, S.G., Chichagov, V.P. & Chichagova, O.A., 1998a. Paleoseismological investigations on the territory of Russian (Gornyi) Altai, *J. Earthquake Prediction Res.*, **7**(4), 391–413.

Rogozhin, E.A., Bogachkin, B.M., Nechaev, Yu.V., Platonova, S.G., Chichagova, O.A. & Chichagova, V.P., 1998b. New evidence of strong earthquakes in the Mountainous Altai Region, *Izvestia, Phys. Solid Earth*, **34**(3), 244–250.

Rogozhin, E.A., Ovsyuchenko, A.N., Geodakov, A.R. & Platonova, S.G., 2003. A strong earthquake of 2003 in Gornyi Altai, *Russ. J. Earth Sci.*, **5**(6), 439–454.

Rosen, P.A., Hensley, S., Peltzer, G. & Simons, M., 2004. Updated Repeat Orbit Interferometry package released, *EOS, Trans. Am. geophys. Un.*, **85,** 35.

Sella, G.F., Dixon, T.H. & Mao, A.L., 2002. REVEL: a model for Recent plate velocities from space geodesy, *J. geophys. Res.*, **107**(B4), Art. No. 2081.

Şengör, A.M.C., Natal'in, B.A. & Burtman, V.S., 1993. Evolution of the Altaid tectonic collage and Palaeozoic crustal growth in Eurasia, *Nature*, **364,** 299–307.

Tapponier, P. & Molnar, P., 1979. Active faulting and Cenozoic tectonics of the Tien Shan, Mongolia and Baykal regions, *J. geophys. Res.*, **84,** 3425–3459.

Thomas, J.C., Lanza, R., Kazansky, A., Zykin, V., Semakov, N., Mitrokhin, D. & Delvaux, D., 2002. Paleomagnetic study of Cenozoic sediments from the Zaisan basin (SE Kazakhstan) and the Chuya depression (Siberian Altai): tectonic implications for central Asia, *Tectonophysics*, **351,** 119–137.

Wright, T.J., Parsons, B.E., Jackson, J.A., Haynes, M., Fielding, E.J., England, P.C. & Clarke, P.J., 1999. Source parameters of the 1 October 1995 Dinar (Turkey) earthquake from SAR interferometry and seismic body-wave modelling, *Earth planet. Sci. Lett.*, **172,** 23–37.

Wright, T.J., Lu, Z. & Wicks, C., 2003. Source model for the M_w 6.7, 23 October 2002, Nenana Mountain Earthquake (Alaska) from InSAR, *Geophys. Res. Lett.*, **30**(18), 1974, doi:10.1029/2003GL018014.

Zwick, P., McCaffrey, R. & Abers, G., 1994. *MT5 Program*, IASPEI Software Library, **4**